DE GRUYTER Open Engineering 2022; 12: 447–452

Research Article

Yofentina Iriani*, Mercyurita Dewi Noviastuti, Risa Suryana, Dianisa Khoirum Sandi and Didier Fasquelle

Pr-doped $BiFeO_3$ thin films growth on quartz using chemical solution deposition

https://doi.org/10.1515/eng-2022-0046
received October 26, 2021; accepted February 10, 2022

Abstract: Bismuth ferrite ($BiFeO_3$) is an interesting multiferroic material due to its ferroelectric properties at room temperature. In this study, $Bi_{1-x}Pr_xFeO_3$ and $BiFeO_3$ films were grown on quartz substrates by the chemical solution deposition method at 600°C of annealing temperature. Variation in molar concentration in $Bi_{1-x}Pr_xFeO_3$ was set (x = 0.03, 0.05, 0.1, and 0.2) to investigate their crystal structure and optical characteristics. $BiFeO_3$ and $Bi_{1-x}Pr_xFeO_3$ films were examined using X-ray diffraction (XRD) and ultraviolet (UV)-vis spectrophotometer. The XRD results demonstrated that the addition of Pr in $BiFeO_3$ shifted the diffraction angle to smaller angles so that it reduced their lattice constant. Besides, the crystal size declined with more Pr numbers, while the lattice strain expanded. The UV-vis characteristics of the films were measured in the wavelength range of 200–800 nm. The transmittance values of the Pr-doped $BiFeO_3$ increased. Because of Pr doping, the refractive index of the $Bi_{1-x}Pr_xFeO_3$ films decreased while the energy dispersion increased.

Keywords: Bismuth ferrite, praseodymium, crystal structure, optical properties, CSD method

1 Introduction

Solar energy is a clean energy source that can be converted directly into electricity by way of a photovoltaic (PV) effect [1]. PV ferroelectrics have gained much interest in the last decade due to their potential in energy conversion [2]. Bismuth ferrite ($BiFeO_3$) has gained special attention from various ferroelectric materials due to its strong ferroelectric properties and bandgap value of ~2.7 eV [3,4]. This small bandgap makes $BiFeO_3$ suitable for PV applications [5,6].

Nevertheless, $BiFeO_3$ possesses drawbacks of high leakage currents, low dielectric constants, and high loss tangents that restrict their applications for device manufacture [7]. To overcome these drawbacks, doping with suitable materials such as rare earth elements at the Bi site, Fe site, or both sites of $BiFeO_3$ can be one of the best solutions. Besides, the doping of rare earth (RE) elements into the $BiFeO_3$ structure can advance its ferroelectric properties [8]. Much research has studied the introduction of RE elements into $BiFeO_3$, including Gd, Ho, Sm, Nd, Eu, and Pr [4,8–12]. $BiFeO_3$ with RE doping, especially Pr, still needs to be developed, primarily because not much work on the optical properties of Pr doped $BiFeO_3$ thin film has been reported.

Further, so far, chemical solution deposition (CSD) or sol-gel method has been frequently used to fabricate the thin film of $BiFeO_3$. It is because the method is simple that it allows better control of the composition of the material and produces a high degree of homogeneity [6,13,14]. Although several studies have reported several experimental works on the preparation of Pr-doped $BiFeO_3$ films, none have reported their growth on quartz substrates.

On these bases, this study focused on the synthesis of $Bi_{1-x}Pr_xFeO_3$ thin film on the quartz substrate using the CSD method. The synthesis was done by varying mole concentration of Pr (x = 0.03, 0.05, 0.1, and 0.2). This study aimed to investigate the effects of various Pr concentration numbers of doping on the crystal structure and optical properties of $BiFeO_3$ and bismuth praseodymium ferrite ($Bi_{1-x}Pr_xFeO_3$) films.

*** Corresponding author: Yofentina Iriani,** Department of Physics, Faculty of Mathematics and Sciences, Universitas Sebelas Maret, Jl. Ir. Sutami 36 A Kentingan Surakarta 57126, Indonesia, e-mail: yofent_iriani@staff.uns.ac.id
Mercyurita Dewi Noviastuti, Risa Suryana, Dianisa Khoirum Sandi: Department of Physics, Faculty of Mathematics and Sciences, Universitas Sebelas Maret, Jl. Ir. Sutami 36 A Kentingan Surakarta 57126, Indonesia
Didier Fasquelle: Department of Unitede Dynamique et Structure des Materiaux Moleculaires, Universite du Littoral-Cote d'Opale, CS 80699F-62228 Calais, France

2 Materials and methods

2.1 Materials

The raw materials used in this research were the sources of Bi, Fe, and Pr, including bismuth(III) nitrate ($(BiNO_3)_3$; Sigma Aldrich, ≥99%), ferrite nitrate ($Fe(NO_3)_3$; Sigma Aldrich, ≥99%), and praseodymium nitrate ($Pr(NO_3)_3$), and the solvents of acetic acid (CH_3CO_2H; Sigma Aldrich, ≥99.7%), 2-methoxyetanol ($C_3H_8O_2$; Sigma Aldrich, ≥99.8%), and acetylacetone (Sigma Aldrich, ≥99.3%).

2.2 Sample preparation

$BiFeO_3$ and $Bi_{1-x}Pr_xFeO_3$ films were deposited on quartz substrates by the CSD method. The first step was making the solutions of $BiFeO_3$ and $Bi_{1-x}Pr_xFeO_3$ ($x = 0.03$, 0.05, 0.1, and 0.2) as follows: the raw materials were weighed according to their respective chemical compositions, the source materials were placed in a beaker and then acetic acid and 2-methoxyethanol were poured, they were stirred continuously using a magnetic stirrer for 60 min, and finally, acetyl acetone was added and stirred for 45 min. The solutions $BiFeO_3$ and $Bi_{1-x}Pr_xFeO_3$ ($x = 0.03$, 0.05, 0.1, and 0.2) were deposited on the quartz substrates using a spin coating with a rotational speed of 3,000 rpm. Moreover, the $BiFeO_3$ and $Bi_{1-x}Pr_xFeO_3$ films were then annealed at a temperature of 600°C. The samples were finally characterized using X-ray diffraction (XRD) and ultraviolet (UV)-vis spectrophotometer to determine the crystal structure and optical properties.

2.3 XRD characterization

Characterization by XRD was to determine the crystal structure of sample $Bi_{1-x}Pr_xFeO_3$. The diffraction patterns were then utilized to compute crystal size, lattice constant, and lattice strain. The lattice constants were calculated using refinement of the General Structural Analysis System software with the Rietveld method and manual calculations. The lattice constant was calculated using equation (1) [15].

$$\frac{1}{d^2} = \frac{4}{3}\left(\frac{h^2 + hk + k^2}{a^2}\right) + \frac{l^2}{c^2}. \tag{1}$$

where d is the interplanar distance, h, k, and l are Miller indices, and a, b, and c are the lattice constants. Meanwhile, the crystal size of the samples was estimated using linear regression by the Scherrer equation and Williamson-Hall methods. For the Scherrer equation, the plot of linear regression could be done by modifying the Scherrer equation as equation (4) [15], where D is the particle size (nm), λ is the wavelength (1.54056 Å), k is a constant equal to 0.94, β_D is the full width at half-maximum intensity (FWHM), θ is the peak position , ε is lattice strain, and β_{hkl} is the FWHM in different condition.

$$D = \frac{k\lambda}{\beta_{D\,\cos\theta}}, \tag{2}$$

$$\beta_D^2 = [\beta^2_{\text{measured}} - \beta^2_{\text{instrumental}}], \tag{3}$$

$$\cos\theta = \frac{k\lambda}{D}\left(\frac{1}{\beta_D}\right). \tag{4}$$

Meanwhile, by using the W–H method, the crystal size could be obtained by the linear regression of the plot of ($\beta_{hkl}\cos\theta$) vs ($4\sin\theta$) as equation (7) [15,16].

$$\beta_{\text{hkl}} = \beta_D + \beta_{\text{strain}}, \tag{5}$$

$$\beta_{hkl} = \left(\frac{k\lambda}{D\cos\theta}\right) + \ (4\varepsilon\tan\theta), \tag{6}$$

$$\beta_{hkl}\cos\theta = \left(\frac{k\lambda}{D}\right) + (4\varepsilon\sin\theta). \tag{7}$$

2.4 UV-vis spectrophotometer

Characterization by UV-vis spectrophotometer provides information on wavelength (λ)-dependent absorbance (A) and transmittance (T). From the transmittance data, the light dispersion and refractive index of the sample $Bi_{1-x}Pr_xFeO_3$ could be found. The formula for determining the refractive index is shown in equation (8) [17]. In which, S is a transmission spectrum, N_1 is a spectral region, T_S is the substrate transmittance, T_m is the sample transmittance, and n is the refractive index. Meanwhile, the light dispersion was determined by the plot of $1/(n^2 - 1)$ vs E^2, where E is the energy determined by equation (11) [2].

$$n = \left[N_1 + (N_1^2 - s^2)^{\frac{1}{2}}\right]^{\frac{1}{2}}, \tag{8}$$

$$N_1 = \frac{2s}{T_m} + \frac{s^2 + 1}{2}, \tag{9}$$

$$S = \frac{2s}{T_m} + \sqrt{\frac{1}{T_s^2}} - 1, \tag{10}$$

$$E^2 = (hv)^2. \tag{11}$$

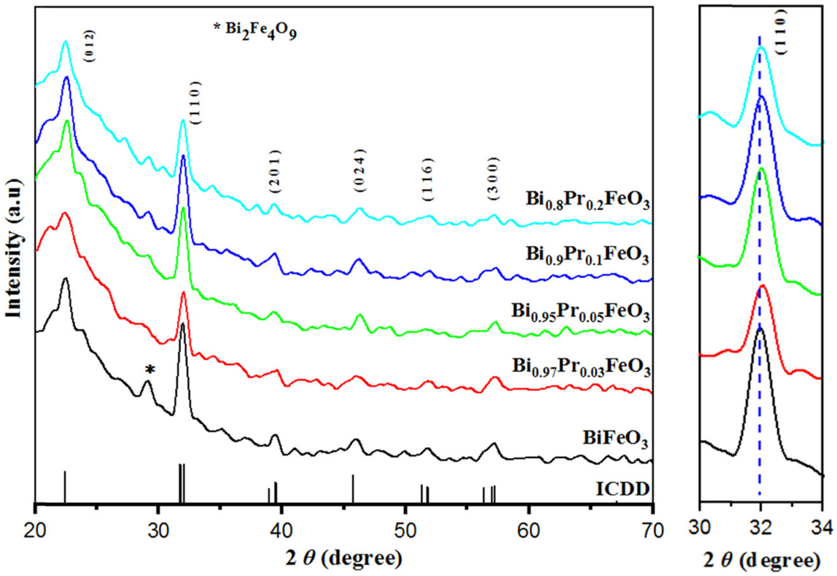

Figure 1: (a) Diffraction patterns and (b) magnification of the main peaks of $Bi_{1-x}Pr_xFeO_3$ films.

3 Results and discussion

Figure 1 shows XRD pattern of $Bi_{1-x}Pr_xFeO_3$ with (x = 0, 0.03, 0.05, 0.1, and 0.2). The diffraction peaks match with $BiFeO_3$ (ICDD) database #861518. Figure 1a shows another phase formed in $BiFeO_3$ (x = 0) pattern that belongs to Bi_2FeO_9 with ICDD database #741098. This impurity is considered because of the immature crystal growth during annealing in the fabrication process. It is similar to the research conducted in ref. [18].

However, for all $Bi_{1-x}Pr_xFeO_3$ samples, other phases were slightly reduced. It suggests that the addition of Pr dopants declines the formation of other phases during the fabrication [18]. Figure 1b shows the magnification of the main diffraction peaks showing that the addition of Pr dopant causes the angles to shift to bigger ones. It is

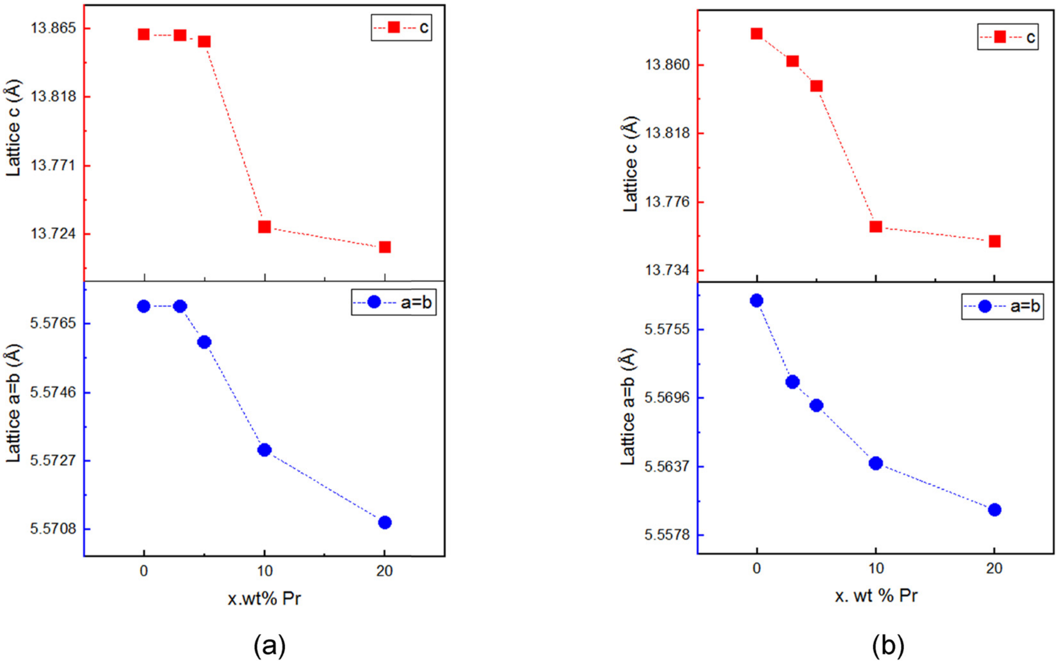

Figure 2: Lattice constants of $BiFeO_3$ and $Bi_{1-x}Pr_xFeO_3$ films using (a) GSAS refinement and (b) manual calculation.

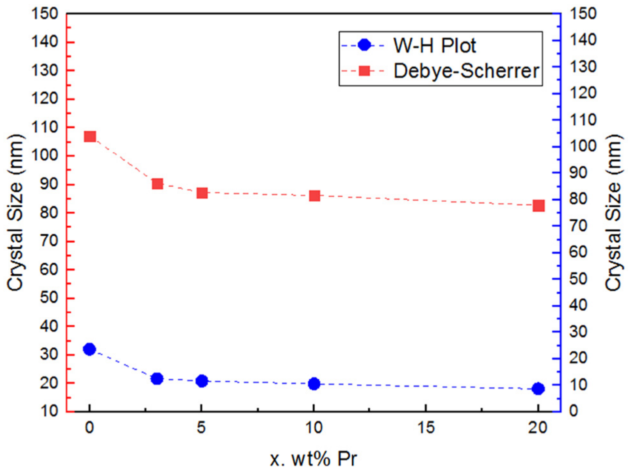

Figure 3: Crystal size of $BiFeO_3$ and $Bi_{1-x}Pr_xFeO_3$ films using William–Hall and Debye Scherrer methods.

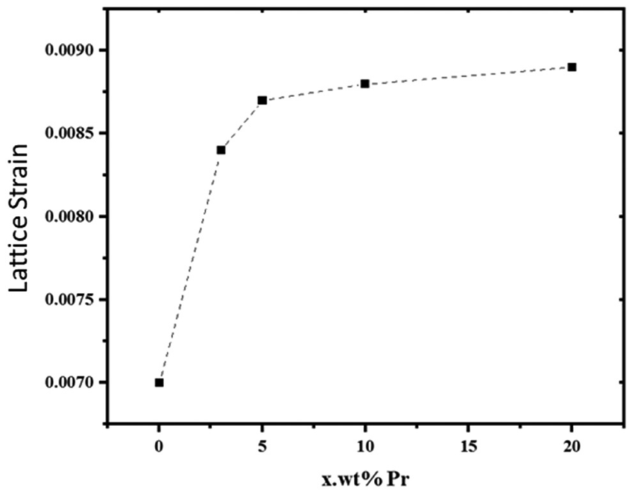

Figure 4: Lattice strain of $BiFeO_3$ and $Bi_{1-x}Pr_xFeO_3$ films.

because the atomic radius of Pr (1.13 Å) replacing the Bi atom (1.17 Å) is smaller [9], which leads to the change in the atomic distance so that the angle shifts toward the bigger theta [19].

Figure 2 exhibits the lattice constant of the $BiFeO_3$ and $Bi_{1-x}Pr_xFeO_3$ films obtained from the GSAS refinement process using Rietveld analysis and manual calculation. The values from the two methods are not significantly different. Besides, based on Figure 2, the addition of Pr in $BiFeO_3$ decreases the lattice constant. It is because the atomic radius of Pr^{3+} (1.13 Å) replacing the Bi^{3+} atom (1.17 Å) is smaller in size [9]. The replacement of the Bi^{3+} atom by $Pr^{3\ +}$ causes the change in the atomic distance, which changes the unit cell volume. However, both using GSAS software and manual calculation, the lattice values are close to the ICDD, where $a = b = 5.577$ Å and $c = 13.861$ Å.

Figure 3 displays the crystal size of the $BiFeO_3$ and $Bi_{1-x}Pr_xFeO_3$ films calculated using Debye Scherrer and William–Hall (W–H) methods. Based on Figure 3, using both methods, the crystal size in the $Bi_{1-x}Pr_xFeO_3$ samples decreases with the increasing Pr doping in $BiFeO_3$. It is stated in [8] that replacing the Ba-site with a smaller ionic radius dopant induces a smaller crystal size. In addition, the replacement of the Bi atom by the Pr atoms results in a change in the unit cell volume, resulting in a small crystal size [34]. However, there is a significant difference in the crystal size values between W–H and Debye Scherrer.

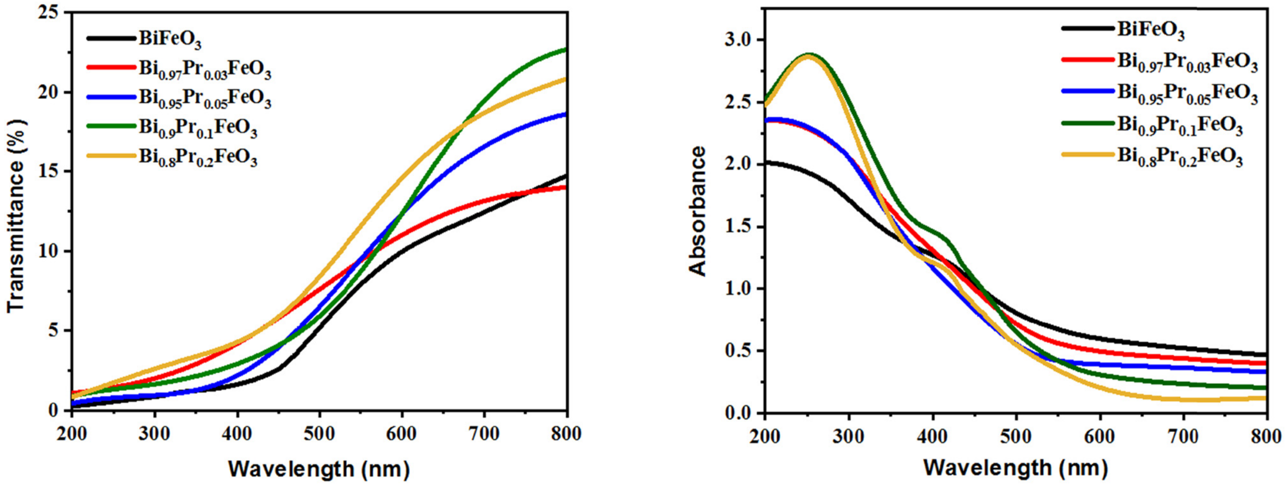

(a) (b)

Figure 5: (a) Transmittance (*T*) and (b) absorbance (*A*) spectra of $BiFeO_3$ and $Bi_{1-x}Pr_xFeO_3$ films.

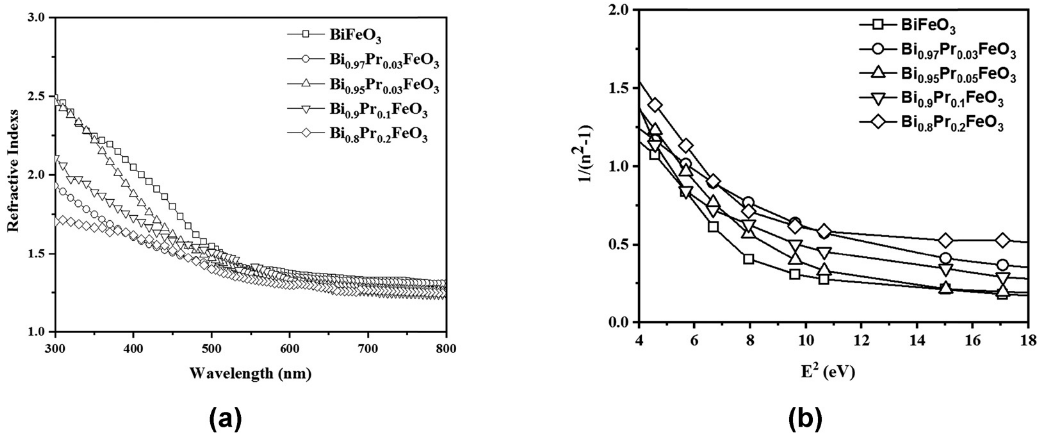

Figure 6: (a) Dispersion energy and (b) refractive index of $BiFeO_3$ and $Bi_{1-x}Pr_xFeO_3$ films.

However, there is a significant difference in crystal size values between W–H and Debye Scherrer. This is because in the W–H plot method there is a correction to the FWHM value, so that the crystal size value using the W–H plot method is smaller than the crystal size value using the Debye Scherrer method. Figure 4 shows the lattice strain of $BiFeO_3$ and $Bi_{1-x}Pr_xFeO_3$ films. It is seen from the figure that the lattice strain advances as the greater number of Pr concentrations. The increment is significantly from 0 to 5% Pr concentration. Here, the lattice strain increases due to the insertion of Pr dopants in the $BiFeO_3$ crystal structure.

Figure 5a shows the transmission values (T) of $BiFeO_3$ and $Bi_{1-x}Pr_xFeO_3$ samples at the wavelengths of visible light in the range of 800–500 nm produce high transmittance (T), and the transmittance value decreases at UV wavelengths in the range of 400–200 nm. This indicates that most of the light energy is transmitted at visible light wavelengths. Meanwhile, Figure 5b presents the absorbance values of $BiFeO_3$ and $Bi_{1-x}Pr_xFeO_3$ samples, which are inversely proportional to their transmittance values, where visible light wavelengths in the 400–200 nm range produce high absorbance values (A), and in the 800–500 nm range, the absorbance value decreases. On the other hand, the sample can absorb sunlight well at UV light wavelengths. With the addition of Pr doping on $BiFeO_3$, the transmittance value tends to increase. This indicates that the number of photons absorbed by the material is less. This confirms that the sample cannot absorb sunlight well at long wavelengths of visible light. This may be related to the lattice constant and the crystal size of the sample. As reported in other ferroelectric materials, decreasing the crystal size can reduce light scattering and increase transmittance [20].

Figure 6a shows the relationship graph of $1/(n^2 - 1)$ vs E^2 (Ev) to determine the light dispersion of the $BiFeO_3$ and $Bi_{1-x}Pr_xFeO_3$ samples. It reveals that the dispersion value is getting higher as the greater number of Pr dopants. The relationship between wavelength and refractive index of the $BiFeO_3$ and $Bi_{1-x}Pr_xFeO_3$ samples is plotted in Figure 6b. At 400–800 nm wavelength, the refractive index values of the $Bi_{1-x}Pr_xFeO_3$ samples are constant at around 1–1.5. The refractive index then increases in the wavelength range of 300–400 nm. Further, the refractive index (n) tends to decline with the increase in the mole number of Pr doping. The decrement is associated with the small crystal size [9]. The small crystal size leads to fewer electrons in the $Bi_{1-x}Pr_xFeO_3$ samples so that the polarization produced is also reduced. Polarization is proportional to the refractive index based on the Lorentz–Lorentz equation [21]. Thus, as the higher Pr doping induces a smaller crystal size, it causes the reduction of the refractive index as well.

4 Conclusion

The films of praseodymium (Pr) doped $BiFeO_3$ or $Bi_{1-x}Pr_xFeO_3$ have been prepared using the CSD method with the mole number of x = 0.03, 0.05, 0.1, and 0.2. The XRD results show that the Pr addition in $BiFeO_3$ causes the diffraction angle to shift to smaller angles so that the lattice constant changes to smaller values. The crystal size also shrinks as the more Pr doping, while the lattice strain expands. Based on the UV-Vis spectrophotometer results, the transmittance spectra increase with the increasing Pr number, indicating that the absorbance spectra decrease. Moreover, the refractive index and light dispersion of the $Bi_{1-x}Pr_xFeO_3$ samples increase with the increase of Pr doping.

Acknowledgments: The authors wish to thank Penelitian Unggulan Terapan 2020 PNBP UNS No. 425/UN27.21/PP/2020 for the financial support.

Funding information: The authors would like to thank Penelitian Unggulan Terapan 2020 PNBP UNS No. 452/UN27.21/PP/2020 for the financial support.

Author contributions: M.D.N.: performance of the experiment; Y.I., R.S., D.K.S.: data analysis and calculation; Y.I., M.D.N., D.K.S., R.S., and D.F.: report writing, translation, and revision. The financial was provided by Y. Iriani. The final report was committed by all contributors.

Conflict of interest: The authors declare that there is no conflict of interest.

References

[1] Gielen D, Boshell F, Saygin D. Climate and energy challenges for materials science. Nat Mater. 2016;5(2):117–20.

[2] Fridkin VM, Popov BN. Anomalous photovoltaic effect in ferroelectrics. Sov Phys Usp. 1978;21(12):981–91.

[3] Charishma, Shastrimath VD, Raghavendra B, Murari MS, Jayarama A, Richard P. Structural, morphological, and optical properties of barium doped bismuth ferrite thin films deposited by spray pyrolysis. Mater Today: Proc. 2021;35:440–4.

[4] Xia W, Pei Z, Leng K, Zhu X. Research progress in rare earth-doped perovskite manganite oxide nanostructures. Nanoscale Res Lett. 2020;15(1):9.

[5] Chen M, Ding J, Qiu J, Yuan N. Effect of film thickness and bottom electrode material on the ferroelectric and photovoltaic properties of sputtered polycrystalline $BiFeO_3$ films. Mater Lett. 2015;139:325–8.

[6] Yao L, Wu X, Yang S, Zhang Y. Structural and optical properties of Ca doped $BiFeO_3$ thin films prepared by a sol-gel metho. Ceram Int. 2017;43:S470–3.

[7] Pattanayak S, Priyadarshan A, Subudhi R, Nayak RK, Padhee R. Tailoring of electrical properties of $BiFeO_3$ by praseodymium. J Adv Ceram. 2013;2(3):235–41.

[8] Zhang F, Zeng X, Bi D, Guo K, Yao Y, Lu S. Dielectric, ferroelectric, and magnetic properties of Sm-Doped $BiFeO_3$ ceramics prepared by a modified solid-state-reaction method. *Materials* (Basel). 2018;11:2208.

[9] Arti, Kumar S, Kumar P, Walia R, Verma V. Improved ferroelectric, magnetic and photovoltaic properties of Pr doped multiferroic bismuth ferrites for photovoltaic application. Results Phys. 2019;14:102403.

[10] Noviastuti MD, Kusumandari, Suryana R, Iriani Y, Fasquelle D. Effects of Nd and Mn Co-dopant on the microstructure and optical properties of $BiFeO_3$ thin films elaborated by chemical solution deposition (CSD). J Phys: Conf Ser. 2021;1825:012060.

[11] Zhang N, Chen D, Niu F, Wang S, Qin L, Huang Y. Enhanced visible light photocatalytic activity of Gd-doped $BiFeO_3$ nanoparticles and mechanism insight. Sci Rep. 2016;6:26467.

[12] Makoed I, Prigodich V, Yanushkevich K, Zhivulko A, Zhivulko V, Galias A, et al. Effect of co-doping on magnetic properties of Bismuth Ferrite. Acta Phys Pol A. 2020;137(5):985–8.

[13] Agustina EB, Iriani Y, Suryana R. Effect of pre-annealing and annealing temperature on microstructural and optical properties of multiferroic $BiFeO_3$ thin films prepared by chemical solution deposition (CSD). J Phys: Conf Ser. 2019;1397:012002.

[14] Haruna A, Abdulkadir I, Idris SO. Photocatalytic activity and doping effects of $BiFeO_3$ nanoparticles in model organic dyes. Heliyon. 2020;6(1):e03237.

[15] Khorsand ZA, Abd, Majid WH, Abrishami ME, Yousefi R. X-ray analysis of ZnO nanoparticles by Williamson–Hall and size–strain plot methods. Solid State Sci. 2011;13(1):251–6.

[16] Birkholz M. Thin film analysis by X-ray scatteing. Germany: Wiley-VCH; 2006.

[17] Swanepoel R. Determination of the thickness and optical constants of amorphous silicon. J Phys E: Sci Instrum. 1983;16:1214–22.

[18] Albino GM, Gálvez-Saldaña M, Perales-Pérez O. Effect of Praseodymium Species on the structural and functional properties of nanocrystalline $BiFeO_3$ powders and thin films. Mater Res Soc Symp Proc. 2012;1454:39–44.

[19] Varshney D, Sharma P, Satapathy S, Gupta PK. Structural, magnetic and dielectric properties of Pr-modified $BiFeO_3$ multiferroic. J Alloys Compd. 2014;584:232–9.

[20] Ranjbar S. Fabrication of bismuth titanate ($Bi_4Ti_3O_{12}$) thin films: effect of annealing temperature on their structural and optical properties. Sci Iran. 2018;26(3):1990–6.

[21] Sharma A, Barman PB. An optical study of vacuum evaporated amorphous $Ge_{20}Te_{80-x}Bi_x$ thin films using transmission and reflection spectra. Appl Phys B. 2009;97(4):835–40.